Generation and dynamics of SOL corrugated profiles

Philippe Ghendrih, Y. Asahi, E. Caschera, Guilhem Dif-Pradalier, P. Peter Donnel, X. Garbet, C. Gillot, V. Grandgirard, G. Latu, Y. Sarazin, et al.

Generation and dynamics of SOL corrugated profiles

IOP Conf. Series: Journal of Physics: Conf. Series **1125** (2018) 012011 doi:10.1088/1742-6596/1125/1/012011

Generation and dynamics of SOL corrugated profiles

P. Ghendrih[1], Y. Asahi[1], E. Caschera[1], G. Dif-Pradalier[1], P. Donnel[1], X. Garbet[1], C. Gillot[1], V. Grandgirard[1], G. Latu[1], Y. Sarazin[1], S. Baschetti[1,2], H. Bufferand[1], T. Cartier-Michaud[2], G. Ciraolo[1], P. Tamain[1], R. Tatali[2], E. Serre[2]

[1] CEA, IRFM, F-13108 Saint-Paul-lez-Durance, France
[2] M2P2, Aix-Marseille Universit, CNRS, F-13451 Marseille, France

E-mail: philippe.ghendrih@cea.fr

Abstract. The staircase transport regime reported in kinetic simulations of plasma turbulent transport in magnetic confinement is recovered with a simple 2D fluid model allowing for reduced damping of the zonal flows. Some of the complex dynamics of the kinetic zonation regime are recovered but the pattern of the corrugation appears to be sinusoidal with a characteristic scale comparable to that of turbulence modes with largest spectral energy, in contrast to regimes observed in global and flux-driven kinetic simulations. Enhanced zonal flows govern both an overall reduction of the SOL width and a gradual steepening of the gradients with distance to the separatrix.

1. Introduction

A major step towards a better understanding of confinement performance has been achieved when more relevant handling of the zonal flow physics [1] has been implemented in turbulent transport simulations [2]. A major difference that has emerged from these studies is that the required temperature profiles to achieve the target amplification factor in ITER [3] appeared to range between the linear and non-linear ITG threshold. In this region of turbulence dynamics, zonal flows self-generated by turbulence have sufficient shearing to strongly inhibit turbulent transport. Exploration of this regime is rather complex since it tends to be quite sensitive to many features such as spreading, collisionality etc. We are interested here in the staircase or corrugation regime [4]. The latter is characterised by the build-up of several shear layers acting as weak transport barriers. These layers are not pinned to specific radial locations and appear to undergo continuous reorganisation and build-up [4, 5]. Between the shear layers, regions governed by so-called avalanche transport develop. This avalanche transport is characterised by ballistic heat transport on long distances coupled to momentum dipoles and Reynolds stress convection. The interplay between the localised shear layers and the avalanching layers is most likely a key feature in determining the geometry and strength of the staircase transport regulation.

Although zonal flow dynamics have been mostly investigated in the kinetic framework for fusion plasmas, they are ubiquitous in quasi 2D turbulence as reported in geophysics and atmospheric physics, where the standard fluid framework is used. Along this line, we investigate here the corrugation dynamics using the simplest available turbulence model in the fluid framework analogous to Rayleigh-Bénard convection [6]. Changes to the vorticity equation allows one to

independently tune the amplitude of the zonal flows and investigate the zonal flow pattern and impact on plasma confinement. The model was initially developed for Scrape-Off-Layer turbulence. Parallel transport to the limiter then governs volumetric losses, which we retain here, but considering a linearised form. By many aspects, these are found to be comparable to parallel loss terms for closed magnetic surfaces. Regarding core heat transport, hence replacing the density field by a temperature field, a similar model can be obtained in the case of strongly radiating layers, a regime of interest in future reactors. However, beyond such speculative projections, one should consider this approach as a tentative representation of the very complex kinetic staircase regime with the simplest available fluid turbulence model in the flux-driven regime. The scope is then to identify the key physics that govern the confinement performance of such a regime. Section 2 of the paper addresses the model together with the linear analysis and the changes introduced to generate corrugations, in Section 3 the simulations in the non-linear transport regime are described and in Section 4 are found the Discussion and Conclusion.

2. Scrape-Off Layer turbulence with flute approximation

2.1. Model for Scrape-Off Layer turbulence

To address the physics of corrugation generation in profiles, and their significance with respect to transport, we address the simplest possible turbulent system, named for simplicity after the code as the TOKAM2D system. This model is developed to describe the interchange instability in the Scrape-Off Layer of fusion plasmas [7, 8]. The system of equations describes the evolution of the electron density n and that of vorticity W. These stem from particle and charge balance equations taking into account the drift expansion solution for the transverse momentum [7]. The vorticity is related to the electric potential ϕ by the relation $W = \nabla_\perp^2 \phi$ in the cold ion limit. For the sake of simplicity a-dimensional equations are considered in $2D$ slab geometry with $x = (r-a)/\rho_0$ and $y = a\theta/\rho_0$, where r and θ are the radial and poloidal coordinates, a the plasma minor radius and ρ_0 the length scale normalisation, namely a characteristic ion Larmor radius.

$$\frac{\partial n}{\partial t} + \Big[\phi, n\Big] - D\nabla_\perp^2 n = S - \sigma_n n\ e^{\Lambda-\phi} \tag{1a}$$

$$\frac{\partial W}{\partial t} + \Big[\phi, W\Big] - \nu\nabla_\perp^2 W = -\frac{g}{\overline{n}}\partial_y n + \frac{\sigma_\phi}{\overline{n}}\ n\ \left(1 - e^{\Lambda-\phi}\right) \tag{1b}$$

Given the flute approximation all fields are averaged along the parallel direction. The poloidal angle is then a transverse coordinate to the field line, in the magnetic surface. The diffusion operators with amplitude D for particles and ν for vorticity stand typically for sub grid processes and include collisional effects for the vorticity (single species collisions do not yield particle transport). The volumetric loss terms with coefficients σ_n and σ_ϕ describe the average parallel loss terms for particles and charges. In the SOL, these losses can be determined by the plasma sheath at the wall boundary, assuming adiabatic electrons in the direction parallel to the magnetic field, and Λ standing for the reference potential jump in the sheath, the wall being grounded. In the sheath theory, one finds that $\sigma_n = \sigma_\phi$. Extending the model, in particular to core physics, we consider these parameters to be independent control parameters, table 1. The Poisson brackets that appear in the two evolution equations stem from the electric drift convection and stand for the divergence of the particle flux and that of the polarisation current. They are defined by: $[\phi, f] = \partial_x\phi\partial_y f - \partial_y\phi\partial_x f$.

In the system (1), one considers constant thermal energies and constant magnetic field, the variation of magnitude of the magnetic field being taken into account by the g term. Expressions for g can be derived [6], it is considered here as a control parameter, for simplicity constant in time and space. The set of equations is homogeneous with respect to the density but for the source term. The density can thus be multiplied by any constant, only leading to a change of

the source amplitude. Conversely, the source normalisation determines the magnitude of the density. This property is specific of density transport and is not recovered when addressing heat transport. The change in symmetry is governed by the fact that the plasma polarisation is proportional to $(n/B^2)\nabla_\perp\phi$ hence to the density and not to the thermal energy. In addition to the flute approximation, reducing the problem to $2D$, we have also used the Boussinesq approximation, leading to the definition of the vorticity introduced above. In this framework, one approximates the density by $\overline{n}$ in the polarisation current, allowing $\overline{n}$ to commute with the divergence operator. In that approximation, $\overline{n}$ is a constant, which is in fact used to normalise the density, therefore setting $\overline{n}=1$ in the equation. We further simplify the system by linearising the parallel loss terms, hence for the density equation $n-\overline{n}(\Lambda-\phi)$ (with $\overline{n}=1$) and for the vorticity equation $-(\Lambda-\phi)$. Since Λ is set to be a constant, one can readily change variable $\phi-\Lambda\rightarrow\phi$.

When extending the model to core physics, and considering a closure of the parallel current of the form $j_\parallel=\sigma_\parallel\nabla_\parallel\phi$, where $\sigma_\parallel$ is the parallel conductivity, one finds that the divergence of the parallel current $\nabla_\parallel j_\parallel$ must vanish with the parallel wave vector $k_\parallel$, equivalently that $\sigma_\phi=k_\parallel^2\sigma_\parallel$. In the flute approximation, the parallel wave vector $k_\parallel$ is replaced by the poloidal wave vector k_y, and, one finds therefore that the restoring force vanishes for $k_y=0$. To take this property into account, we must therefore modify the equation that governs the average potential $\langle\phi\rangle$. A priori, this average is a flux surface average removing divergences of parallel flux terms; in the present model the average is along the poloidal coordinate y. In order to take into account the change in restoring force for $\langle\phi\rangle$ compared to other modes $k_y\neq0$, we introduce a further control parameter α_z and modify the volumetric charge loss: $\sigma_\phi\phi\rightarrow\sigma_\phi(\phi-(1-\alpha_z)<\phi>)$. With these simplifications and changes one can step to the following set of equations:

$$\frac{\partial n}{\partial t}+\Big[\phi,n\Big]-D\nabla_\perp^2 n=S-\sigma_n n \tag{2a}$$

$$\frac{\partial W}{\partial t}+\Big[\phi,W\Big]-\nu\nabla_\perp^2 W=-\frac{g}{\overline{n}}\partial_y n+\sigma_\phi\Big(\phi-(1-\alpha_z)\left\langle\phi\right\rangle\Big) \tag{2b}$$

The effect of the control parameter α_z is discussed in Section 2.3. Most of the modelling effort of SOL and divertor physics assumes flux-driven regimes, hence in the present case a prescribed mean particle flux driven by the source term S [6]. Results that have been obtained underline the importance of the non-linear features in the dynamics of the system. However, as a guideline to investigating the physics, it is interesting to consider the response to a prescribed gradient as done in standard linear analysis.

2.2. Linear analysis

A key aspect in the linear analysis is the choice of the reference state that is investigated. We assume here that this state is defined as being constant in the poloidal direction and that its evolution in time is small compared to the growth rate that is computed. For the sake of simplicity we consider a reference density gradient $L_n^{-1}=|\nabla_x n|/\overline{n}$ with no structure of the electric potential, hence setting the latter to zero. The evolution of the mean values is addressed in the next subsection. For the other modes, the analysis in Fourier space then yields the dispersion relation where ω_R is the mode frequency and γ the mode growth rate:

$$\Big(\omega_R+i\big(\gamma+\tfrac{1}{2}(A_n+A_\phi)\big)\Big)^2+B=0 \tag{3a}$$

$$A_n=Dk^2+\sigma_n \quad ; \quad A_\phi=\nu k^2+\sigma_\phi/k^2 \tag{3b}$$

$$B=C-A_nA_\phi+\tfrac{1}{4}(A_n+A_\phi)^2 \quad ; \quad C=\frac{g}{L_n}\frac{k_y^2}{k^2} \tag{3c}$$

The coefficients A_n and A_ϕ govern the damping in the density and vorticity, equations. They depend on the wave vectors in the x and y directions, k_x and k_y respectively, and on $k^2 = k_x^2 + k_y^2$. By convention negative values of the growth rate γ govern mode damping. For $C \geq 0$, one finds $B \geq 0$ so that the dispersion equation can readily be split into real and imaginary part since all coefficients are real. One then obtains $\omega_R = 0$ and therefore the largest growth rate γ_+:

$$\gamma_+ = -\tfrac{1}{2}(A_n + A_\phi) + B^{1/2} \tag{3d}$$

Consequently the instability threshold condition, $\gamma_+ = 0$, is determined by $B \geq \frac{1}{4}(A_n + A_\phi)^2$, which can be written as $C \geq A_n A_\phi$. Scanning the values of the wave vector k_y, one then finds a maximum value of L_n such that $\gamma_+ \leq 0$ and is equal to zero at the maximum. To simplify the analysis we define the anisotropy ratio $a_{xy} = k_x^2/k_y^2$ as a control parameter so that one can analyse the threshold and marginality with respect to k_y^2 or $k^2 = k_y^2(1 + a_{xy})$. Defining the function $G(k^2) = k^2(A_n A_\phi - C)$, the instability condition is then $G(k^2) \leq 0$ and the marginality condition when varying k, equivalently k_y, is $\partial_{k^2} G(k^2) = 0$. One can show that:

$$G(k^2) = \frac{k^2}{2}\partial_{k^2} G(k^2) + \frac{\nu\ \sigma_n}{2k^2}\Big(k^4 + 2\ \frac{D\sigma_\phi - C}{\nu\ \sigma_n}\ k^2 + \frac{3\sigma_n\sigma_\phi}{\nu\ \sigma_n}\Big) \tag{4a}$$

The threshold $G(k^2) = 0$ and marginality $\partial_{k^2} G(k^2) = 0$ conditions then lead to a second order equation and the constraint on C to obtain the unique critical root is then:

$$C_* = D\ \sigma_\phi + \sigma_n\sqrt{3\nu\ \sigma_\phi} \tag{4b}$$

$${k_*}^2 = \sqrt{3\frac{\sigma_\phi}{\nu}} \tag{4c}$$

In these expressions the control parameter C is defined as $C = g\ L_n^{-1}/(1 + a_{xy})$. It does not depend on k^2 but on the control parameters g, L_n and a_{xy}. These only appear in C leading to similarity properties. Considering the threshold to anisotropic turbulence, one has $1/L_n^* = C_*(1 + a_{xy})/g$, namely the critical gradient increases for a decreasing anisotropy of "streamer-like" structures, $k_x \leq k_y$, $0 \leq a_{xy} \leq 1$, and it also increases for a growing anisotropy of "zonal-like" structures $k_x \geq k_y$, hence $a_{xy} \geq 1$. It is to be underlined that the scale separation between the gradient length and the mode wave vector can only be assumed for $k_x L_n \gg 1$. The present analysis therefore implicitly assumes a lower bound on the value of k_x.

The critical value k_* translates into a critical value of k_y^* at given turbulence anisotropy. The linear analysis thus yields two different scales, the macro scale L_n for the self-organised profiles and the micro scales λ_y^* that governs turbulent properties, typically $\lambda_y^* = 2\pi/k_y^*$ of the most unstable mode for given k_x. It is to be noted that the asymmetry between radial and poloidal directions is only due to the ratio k_y^2/k^2 in C, equation (3c). For the chosen values of the control parameters, see table 1, setting $k_x = 0$, hence $a_{xy} = 0$, the critical gradient is then found to be $L_n^* \approx 478\rho_0$ and drives modes with poloidal wave length $\lambda_y^* = 2\pi/k_y^* \approx 39\rho_0$. Such a critical gradient length is comparable to the radial extent of the simulation domain that has been used, $L_x = 512\rho_0$.

Two aspects are found to play an important role in the behaviour of the system, the drive governed by C and the damping characterised by $A_n A_\phi$, which exhibits a dependence in k^2. The inverse of this function determines the region of minimum damping, therefore the most favourable region for instability development. On Figure 1, the damping rates A_ϕ, blue plain line and open circles, and $A_n A_\phi$, black plain line closed circles, are plotted versus k. The minimum is governed by the specific structure of A_ϕ combining a monotonically increasing viscous damping νk^2, blue dashed line, and the monotonically decreasing damping σ_ϕ/k^2, thin

Table 1. Reference values of the control parameters in equation (2).

D	ν	σ_n	σ_ϕ	g	α_z	a_{xy}
10^{-2}	2^{-2} 10^{-2}	2^{-14}	2^{-16}	10^{-4}	1	1

blue plain line. Interestingly enough, the minimum of A_ϕ, at $k^4 = \sigma_\phi/\nu$, is close to the critical value given in equation (4c). The impact of A_n, on the product $A_n A_\phi$, thin plain lines and closed circles, is to shift the minimum to lower k and make it more hollow: hence more discriminating for instability onset. The damping properties thus favour a characteristic wave vector k for the instability, and, for a given k, the larger k_x the smaller the associated k_y. The term C, equation (3c), is proportional to the density gradient length L_n that obviously will scale with g. As already discussed, this term also exhibits a symmetry breaking between poloidal and radial wave vector, the larger k_x the smaller the ratio k_y^2/k^2 and thus the critical gradient length.

Considering the points (γ^c, L_n^c, λ_y^c), namely the maximum growth rate γ^c, associated to mode wave length λ_y^c for a given density gradient length L_n^c, one can extend the discussion for the critical onset of instabilities to that with finite growth rate, Figure 2. For increasing values of the growth rate, one finds that the density gradient length required to trigger the instability decreases close to exponentially, Left Hand Scale, blue plain line for $k_x = 0$, $a_{xy} = 0$, and dashed black line for $k_x = k_y$, $a_{xy} = 1$. Note that this dependence on k_y^2/k^2 governs the factor 2 difference between the required density gradient length of these two cases. This factor is determined by the value of the ratio of $1 + a_{xy}$ when going from $a_{xy} = 0$ to $a_{xy} = 1$. The corresponding instability wave length is plotted on Figure 2 Right Hand Scale for $k_x = 0$ $a_{xy} = 0$ blue plain line and open triangles, and $k_x = k_y$ $a_{xy} = 1$ black plain line closed triangles. It tends to decrease with increasing growth rate but this decrease is very small and flattens out with γ.

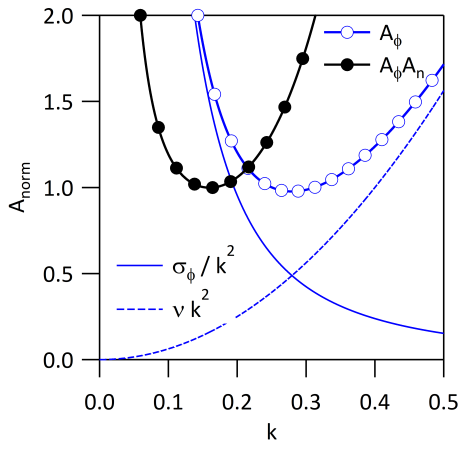

Figure 1. Contributions to mode damping, equation (3c) versus wave vector k. The terms are normalised to the minimum value of A_ϕ or $A_n A_\phi$ to fit the on same graph.

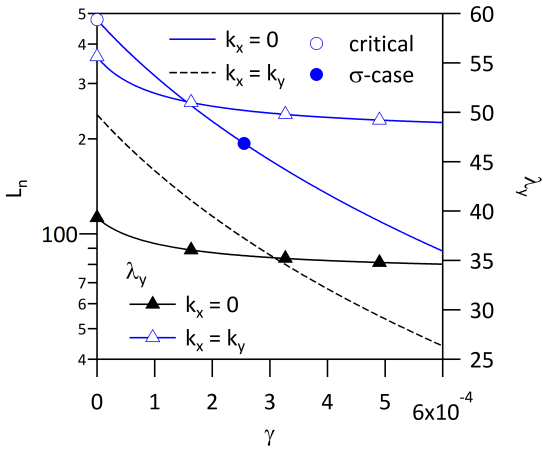

Figure 2. For increasing growth rate γ, variation of the required gradient L_n, Left Hand Scale and of the wave length λ_y of the most unstable mode, Right Hand Scale.

The ratio between the most unstable mode with $k_x = 0$ and the homogeneous case $k_x = k_y$ is a factor $\sqrt{2}$, consistently with the values of the ratio $k/k_y = \sqrt{1 + a_{xy}}$.

2.3. Flux-surface-averaged fields

In the present model, in the flux-driven regime and outside the source region, the flux-surface-averaged fields $\langle n \rangle$, $\langle \phi \rangle$ and $\langle W \rangle = \partial_x^2 \langle \phi \rangle$, have no source but the non-linear coupling between turbulent modes.

$$\frac{\partial \langle n \rangle}{\partial t} + \partial_x \left\langle -\widetilde{n} \partial_y \widetilde{\phi} \right\rangle - D \partial_x^2 \langle n \rangle = \langle S \rangle - \sigma_n \langle n \rangle \tag{5a}$$

$$\frac{\partial \langle W \rangle}{\partial t} + \partial_x \left\langle -\widetilde{W} \partial_y \widetilde{\phi} \right\rangle - \nu \partial_x^2 \langle W \rangle = \alpha_z \sigma_\phi \langle \phi \rangle \tag{5b}$$

The flux-surface-averaged vorticity $\langle W \rangle$ is the shear of the zonal flow $V_z = \partial_x \langle \phi \rangle = \langle v_{Ey} \rangle$. The z subscript for V_z and α_z refers to zonal flows. Taking this definition into account, one can write an alternative form for equation (5b):

$$\partial_x \Big(\frac{\partial V_z}{\partial t} + \partial_x R_s - \nu \partial_x^2 V_z \Big) = \alpha_z \sigma_\phi \langle \phi \rangle \tag{5c}$$

where R_s is the Reynolds stress tensor $R_s = \left\langle -\partial_x \widetilde{\phi} \partial_y \widetilde{\phi} \right\rangle$. The structure of this equation is remarkable insofar that is exhibits two damping terms and is such that the only possible drive is via the non-linear contribution, namely the Reynolds stress. Similarly for the particle transport equation (5a), apart from the source term, homogeneous in y and Gaussian in x with half-width 8.5 ρ_0 and localised at $x = 0$, there is no other source but the non-linear turbulent radial particle flux $\Gamma_x = n v_{Ex}$ where v_{Ex} is the x component of the electric drift velocity. In flux-driven systems, the reference background state is generated self-consistently by non-linear constructive interferences of fluctuations. These can act as sources or sinks. However, in contrast, all other terms are sink terms. Numerical simulations are used to address the development and statistical steady state of the mean fields. Before analysing these results, a final remark can be made on the use of the parameter α_z that governs the volumetric damping of $\langle \phi \rangle$ via a restoring force towards $\langle \phi \rangle = 0$. While σ_ϕ governs the damping rate of all modes $k_y \neq 0$, damping of the flux-surface-averaged field is reduced when setting $0 \leq \alpha_z \leq 1$. Introducing such a control parameter aims at both adapting fluid codes to a better handling of zonal flows, as well as modifying the behaviour of the zonal flows in kinetic codes in the adiabatic electron limit. Indeed, the limit $\alpha_z \to 0$, i.e. no restoring force, seems to overestimate zonal flows in kinetic codes leading in some cases to a very stiff barrier response [9, 10].

3. Numerical simulations of SOL turbulent transport

3.1. Reference case of damped zonal flows

Simulations are performed with the TOKAM2D code that has been extensively verified, in particular with the novel PoPe scheme [11]. We analyse here steady state regimes with $\alpha_z = 1$ on a time window corresponding to 30 SOL characteristic time, the inverse of σ_n with the present definitions. The mean density profile is plotted on Figure 3, plain-thick black curve in log-scale. The radial simulation domain on this figure is slit into 3 regions, the source being centred on $x = 0$. The first region, on the Left Hand Scale from $x = 0$ to $x \approx 340$, is characterised by a close to exponential density decrease. Since the simulation domain is periodic, the third region, on the Right Hand Scale, must exhibit a positive, therefore stable gradient. The second region, close to $x = 400$, in a region of turbulence spreading with weaker g-drive due to the decrease and inversion of the density gradient. The maximum and minimum density profiles, due to the fluctuations during the analysed statistical steady time window, are also shown, thin

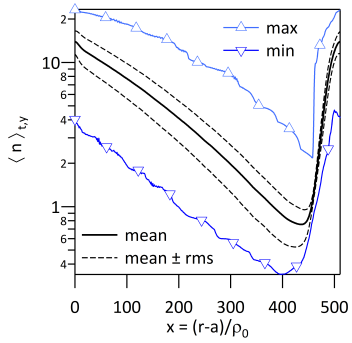

Figure 3. Mean density profile $\langle n \rangle_{y,t}$, maximum and minimum value profiles as well the mean density $\pm$ its rms.

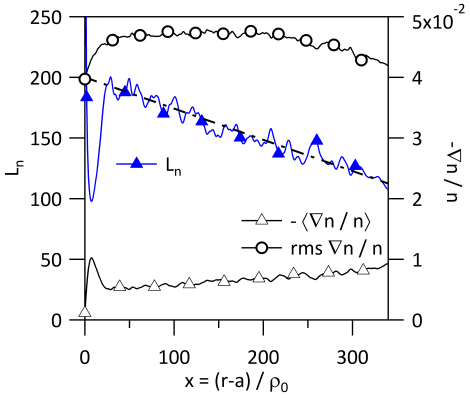

Figure 4. Profile of $L_n^{-1} = \langle -\nabla_x n/n \rangle$ and its rms, Right Hand Scale, and profile of L_n, Left Hand Scale.

blue curves with open up-triangles for the maximum and open down-triangles for the minimum. One observes bumps in these profiles that are indicative of where large avalanche-like transport events have stopped. Convergence towards smoothed-out curves requires very large statistics. They have been found to be particularly slow in such intermittent simulations [12]. Potentially, the realisation of convergence towards statistical steady state of turbulence given such long transients can be impeded by the evolution of other processes leading to global changes on shorter time scales. The density profile is completed by the plot of the mean profile $\pm$ the root mean square (rms) of the density fluctuations, black dashed line. The rms can be observed to be rather constant, while the density decreases, leading therefore to an increase of the relative fluctuation level. The latter increases almost linearly from 20 % to 40 % for x ranging from 0 to 340. For the profiles in the stable region, the rms is squeezed to a small value as readily expected for weak spreading capability.

To complete the analysis of this mean density profile, we consider the density gradient length defined as $L_n = \langle -\nabla_x n/n \rangle^{-1}$, as well as its inverse $1/L_n = \langle -\nabla_x n/n \rangle$ and the rms of the fluctuations of $\nabla_x n/n$, Figure 4. In contrast to the smooth aspect of the mean density profile, one finds that L_n is not smooth, plain line with closed triangles, Left Hand Scale. One can however identify a clear trend characterised by a decrease of L_n by a factor close to 2, a change that is quite significant in view of the sensitivity of divertor operation to this scale, from 200 at $x \approx 25$ to ≈ 100 at $x = 340$. Between $x = 0$ and $x \approx 25$, typically the source region, there is a marked decrease of L_n down to ≈ 100. This analysis indicates that the physics that govern the SOL width are more complicated than described by a single e-folding length, and require detailed and precise measurements to recover experimentally these properties. The profile of L_n^{-1} that is effectively computed, Figure 4 plain line and open triangles Right Hand Scale, is presented for the sake of comparison to its rms. One finds that the latter is characterised by a rather flat profile, plain line, thick open circles and Right Hand Scale, and is typically four times larger than the mean value. The Probability Distribution Function (PDF) reflects this property, the maximum probability is observed at $\nabla_x n/n = 0$, the mean value L_n^{-1} stands in its vicinity and heavy tails, decaying more or less exponentially, skewed towards the positive value of $-\nabla_x n/n$ are observed. Given the very large fluctuation level, relating these mean-field properties to the linear analysis of Section 2 cannot be justified. However, one can consider that it provides a qualitative guideline when investigating the non-linear, highly intermittent SOL transport. For isotropic turbulence $k_x = k_y$ the upper value of L_n, $L_n \approx 200$ is just above marginality while

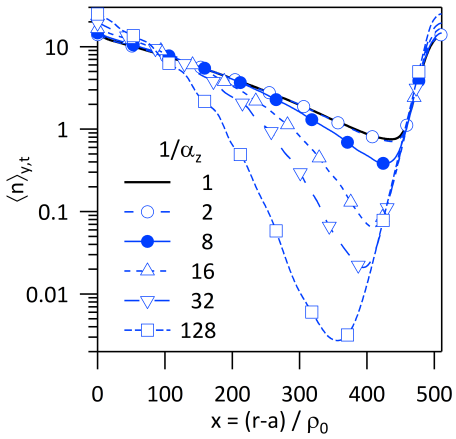

Figure 5. Mean density profile $\langle n \rangle_{y,t}$ with scan of the parameter α_z in equation (5c).

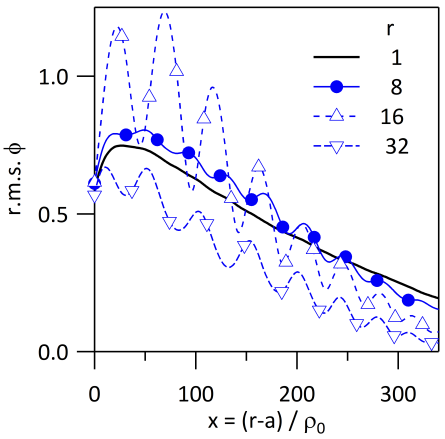

Figure 6. Profiles of the rms of potential fluctuations with α_z-scan.

$L_n \approx 100$ yields a growth rate 2.5 10^{-4}, comparable to σ_n, table 1. The physics suggested by these numbers is that turbulence self-organises to generate marginal e-folding profiles in the vicinity of the source. The decrease of the particle flux governed by the volumetric losses would then require a larger turbulent drive, hence reduced density gradient length. It seems therefore possible to relate the mean-field properties to the linear analysis. More systematic comparison is however required to investigate if such an interpretation, analogous to that proposed for neutral fluids in reference [13, 14], can be used to analyse the SOL width.

3.2. Impact on SOL transport of zonal flows damping rate

Is has been recognised that fluid models are characterised by over-damping of the zonal flows [1, 2]. In that perspective, a first attempt to adapt the TOKAM2D fluid simulations, consisted in reducing the viscous damping of this mode. Although a small effect was noticeable, the overall impact did not lead to a behaviour in agreement with kinetic simulations. A more interesting result has been obtained when introducing the parameter α_z governing the restoring force of the small k_x zonal modes, equation (5c) [15]. From the macroscopic point of view changing α_z reduces significantly the SOL width, Figure 5. As a consequence the reversal of the mean density gradient is shifted towards the small values of x as α_z is decreased. This is a consequence of the numerical implementation with periodic conditions in x. The improved confinement also leads to an increase of the maximum value of the density, enhancing the volumetric particle losses in the source region. For the smallest value of α_z, $\alpha_z = 1/128$, the density at the minimum is close to zero, more than 10^3 times smaller than at $x = 1$, and the profiles tends to be more symmetric in the vicinity of the minimum. In such a case, the profile is governed by diffusion since turbulent transport is quenched. The latter effect is noticeable on the profiles of the potential fluctuations, characterised by the rms, Figure 6. One can observe a decrease of the fluctuation level, governed in first place by the decrease of the density. For $\alpha_z = 1/128$ the relative density fluctuation, rms divided by the mean, is reduced to less than 10^{-2} at the minimum, typically a factor 100 smaller than the value before entering the stable region. The other important feature of the *rms*-profile of the electric potential is the development of modulations, Figure 6. These become visible for $\alpha_z = 1/8$, are largest for $\alpha_z = 1/16$, and then appear to decrease for $\alpha_z \leq 1/32$. Interpretation of this fluctuation level is rather complicated since it combines variations in x and in y that can have different impact on turbulent transport. Regarding the radial flux Γ, one finds a decrease

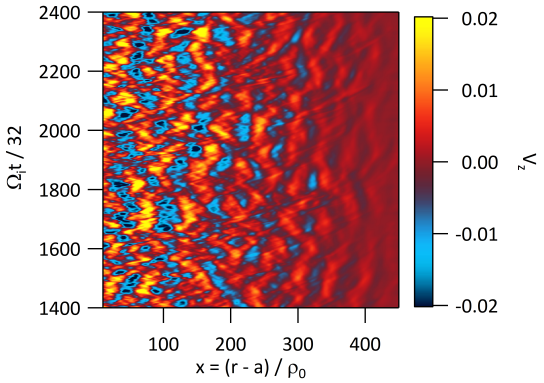

Figure 7. Zonal flow $V_z = \langle v_{Ey} \rangle_y$ versus radial position and time for the reference case $\alpha_z = 1$, no specific zonal flow damping.

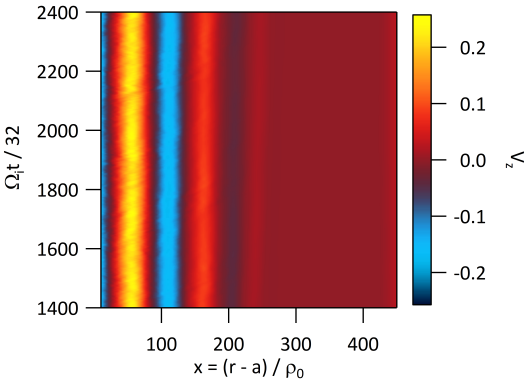

Figure 8. Zonal flow $V_z = \langle v_{Ey} \rangle_y$ versus radial position and time for $\alpha_z = 1/128$, a case with large reduction of zonal flow damping.

with decreasing α_z but less pronounced modulation.

3.3. Zonal flow pattern and generation

The trace of the zonal flow profile is shown in the 2D plot of Figure 7 in the standard case with $\alpha_z = 1$, and Figure 8 for $\alpha_z = 1/128$. Note that the time units on the figures is 32 Ω_i^{-1} that corresponds to the diagnostic stepping. For $\alpha_z = 1$, a pattern with characteristic magnitude 0.02 c_s where c_s is the sound speed, and with rapid reorganisation in time and radial position x is noticeable. The typical wave length is 50 ρ_0. Several time scales can be identified. These typical times appear to become longer when increasing the distance to the source. A characteristic time scale in the region at $x \approx 50$ is roughly 640 Ω_i^{-1}. In contrast, for $\alpha_z = 1/128$, one can observe a regular pattern, Figure 8. The magnitude of the zonal flows V_z is more than a factor 10 larger and exhibits close to equally spaced reversals. The amplitude of the zonal flows $|V_z|$ decays as the distance to the source increases. Zooming on the first maximum of V_z, Figure 9, reveals however short time scale changes that are reminiscent of the reorganisation reported

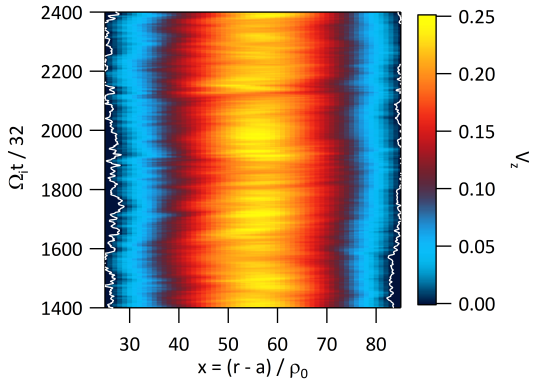

Figure 9. Radial zoom of Figure 8 on the first maximum, $x \approx 55 \pm 30$. The white contour line correspond to $V_z = 0$.

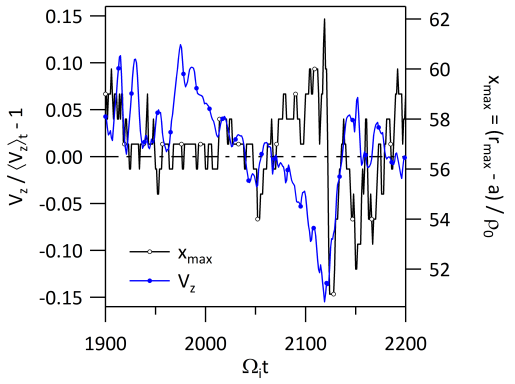

Figure 10. Trace of the evolution of the maximum of V_z on the structure radial extent and of its radial location.

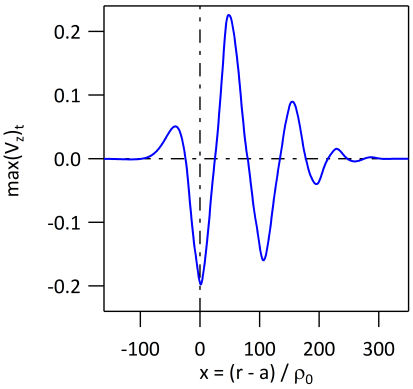

Figure 11. Mean zonal flow profile $\langle V_z \rangle_t$ for $\alpha_z = 1/128$. The origin is shifted with $x \leq 0$ stable and $x \geq 0$ unstable, the source is centred on $x = 0$.

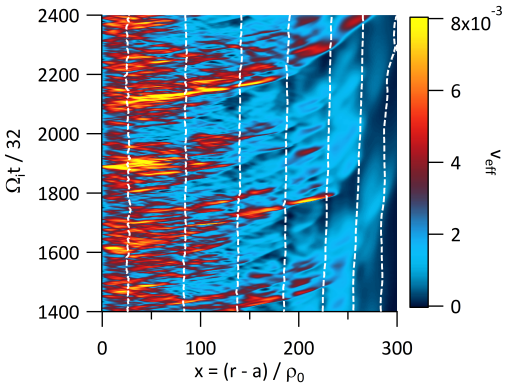

Figure 12. Effective ballistic transport velocity, the dashed white lines localise the zero contour of the zonal flow pattern, in the vicinity of the maximum shear.

for gyrokinetic simulations [5, 16, 17]. They appear as inward or outward ballistic propagation of either minima or maxima with a typical velocity of 0.04 c_s. This range of Mach number, comparable to that of the zonal flow in the case $\alpha_z = 1$, is characteristic of SOL intermittent avalanche transport [18]. Considering the variation of the maximum of V_z in the range $30 \leq x \leq 80$ relative to the time average value, Figure 10 plain blue curve with closed circles, one can observe time dependent fluctuations up to the 10 % range, with relaxation like events. The radial position of the maximum also appears to fluctuate, also in the 10 % range relative to the half width of the zonal flow maximum structure (50 ρ_0). In some cases, anti correlation between position and amplitude can be observed, but this is not systematic. On longer time scales, one can also notice a drift of the position of this zonal-flow structure away from the source. The mean zonal flow profile is shown on Figure 11. Note that the x-axis is shifted. The region left to the source maximum (at $x = 0$), is stable and only exhibits small fluctuations. The pattern is that of a standing wave with asymmetric damping, the fall-off being on a shorter distance in the stable region. The structure on Figure 11 could suggest that the phase of the pattern is locked to that of the source since a minima coincides with $x = 0$. In fact longer simulation times are characterised by slow drifts of the extrema and possible reorganisation of the pattern. However, it seems that the zonal flow structure is constrained and either a minima or maxima is aligned on $x = 0$ at the source maximum. The phase of the wave-like pattern at $x = 0$ thus tends to increase in jumps of π. Such a wave-like pattern, and the development of the mode in the stable region, is indicative of a global structure which appears to be "more linear" than the self-organised pattern reported in gyrokinetic simulations. The physics of this difference in behaviour is still unclear. One can also notice that the wave length is in the range of 100 ρ_0, hence about twice that reported for $\alpha_z = 1$. This could be understood by the fact that the minimum damping region is shifted to higher wave length, by a factor 2.4 for $\alpha_z = 1/128$, together with a reduction by a factor 10 at the minimum damping.

Regarding the decrease of the pattern in the radial direction, it can be explained by the turbulence reduction in the radial direction. Let us consider the effective velocity of transport defined by $V_{eff}(x,t) = \langle \Gamma_x(x,y,t) \rangle_y / \langle n(x,y,t) \rangle_y$, Figure 12, where $\Gamma_x(x,y,t)$ is the turbulent particle flux taking into account the correlation between density and potential fluctuations. Dividing by the average density allows one to remove the obvious impact of the density level on the

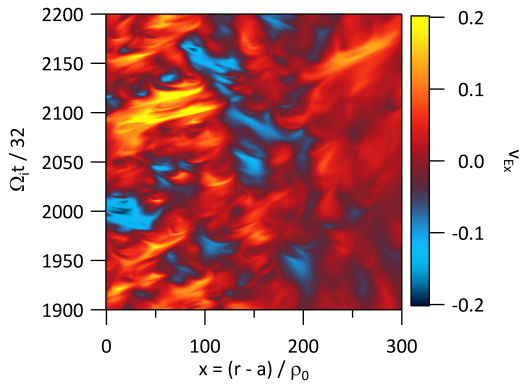

Figure 13. Radial component of the electric drift velocity v_{Ex} at given poloidal position versus radius x and time t for the reference case $\alpha_z = 1$.

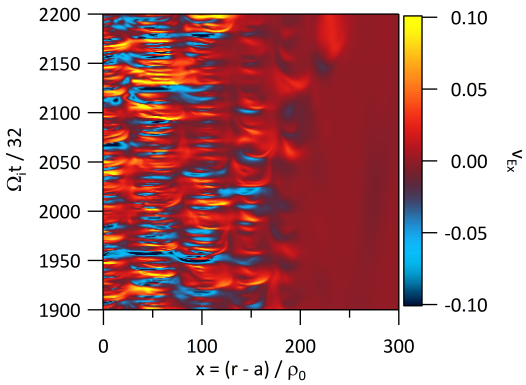

Figure 14. Radial component of the electric drift velocity v_{Ex} at given poloidal position versus radius x and time t for the case $\alpha_z = 1/128$.

particle flux. As obtained is previous SOL turbulence simulations [6], one readily notices events with ballistic radial transport. In this plot the vertical dashed white lines locate the contours with vanishing zonal flow $V_z = 0$, that indicate approximately the position of maximum shear layers. The structure of the zonal flow pattern tends to decrease the number of such events in the course of the radial propagation by introducing a delay and a filtering process of the events with smallest magnitude. Using the ratio of the turbulent radial particle flux divided by the total particle flux (diffusive and turbulent) as done in reference [19] does provide a means to identify transport barrier features. However, the volumetric loss term for the density, which is enhanced by the barrier, as pointed out in [19], tends to limit the build-up of large density gradients at the barrier location so that the effect appears to be quite small using this criterion. In fact, the most noticeable difference between the case with zonal flows and the reference case with over-damped zonal flows appears to be the duration of the transport event and the repetition rate of the avalanche transport events. For $\alpha_z = 1$, the avalanche events are very frequent, and appear to exhibit long radial range when considering the y-averaged transport.
Analysing the radial component of the electric drift velocity v_{Ex} at given poloidal position versus radius x and time t, for $\alpha_z = 1$ Figure 13, compared to $\alpha_z = 1/128$ Figure 14, one also notices that the duration of the structures in the potential with outward velocity, respectively inward, is much shorter with large zonal flow amplitude. Furthermore, v_{Ex} tends to decrease in the large shear region, Figure 14. At times with heads-on directions of v_{Ex} in neighbouring zonal flow structures, these tend to cancel out large scale transport. The reduced duration of time windows such that v_{Ex} is aligned in the neighbouring zonal flow structures also reduce the efficiency of transport at large scale. These two mechanisms can be partly understood as the impact of zonal flow shearing on streamer like transport structures.

Finally, analysing the onset of the zonal flow structure, Figure 15 for $\alpha_z = 1$ and Figure 16 for $\alpha_z = 1/128$, one can notice that the specific properties of the patterns set in very rapidly after the linear phase, typically from $\Omega_i t = 0$ to $\Omega_i t/32 = 100$. For $\alpha_z = 1$ the zonal flow pattern seems to build according to the selection that takes place during the linear phase, hence favouring the idea of a structure determined by the damping process. For $\alpha_z = 1/128$, it seems that at the end of the linear phase, the structure of the zonal flow is comparable to that for $\alpha_z = 1$, and that the pattern then builds via a merging of two structures, as in [20], followed by a radial displacement and further increase of the radial extent, Figure 16.

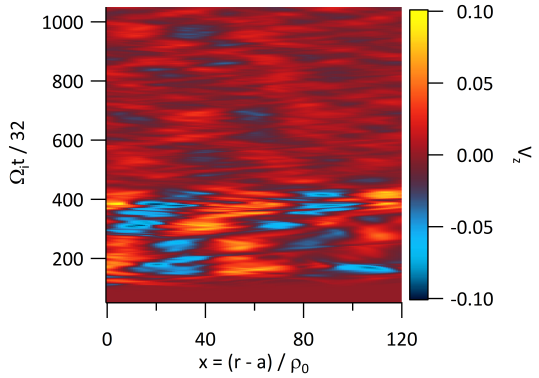

Figure 15. Build-up of the zonal flow radial profile from the linear regime into the non-linear regime, transition typically at $\Omega_i t/32 \approx 100$. Case with large restoring force, $\alpha_z = 1$, and consequently fast reorganisation in space of the zonal flow pattern is readily observed.

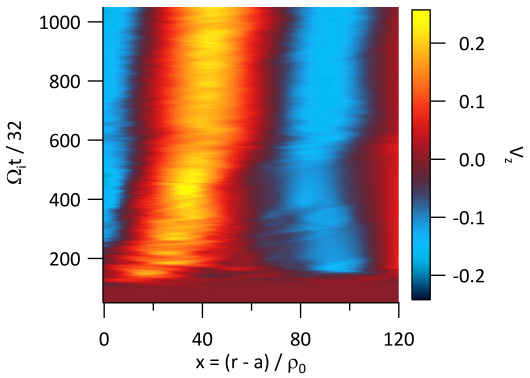

Figure 16. Build-up of the zonal flow profile from the linear regime into the non-linear regime, case with small restoring force, $\alpha_z = 1/128$. Large scale and slow reorganisation is observed with possible structure merging towards the end of the linear phase.

4. Discussion and Conclusion

With relatively small changes of the initial SOL turbulence model we have recovered a regime with corrugated profiles [16, 17, 21]. In this regime, transport is regulated by zonal flow shear layers distributed radially in the plasma volume. The control parameter that determines the amplitude of the zonal flows allows one investigating a large class of regimes. In the reference case, where zonal flows are damped similarly to all modes, one finds a regime with rather homogeneous turbulence and a scrape-off layer that can appear to be characterised by an exponential e-folding length. The precise investigation shows that zonal flows are generated, but at too low amplitude and with too fast reorganisation in time and space to generate patterns that can be identified on transport meso-scales. In that reference regime, with the same restoring force for all modes of the system, one finds that the e-folding length decreases up to a factor 2 as the radial distance from the source is increased. When reducing the restoring force for the zonal flows, the SOL e-folding length is reduced and exhibits a larger variation in the radial direction. It is interesting to note that in the reference case, the mean gradient achieved in the non-linear turbulent regime, and close to the source, coincides with the critical gradient for homogeneous turbulence ($k_x \approx k_y$). This could be indicative that some of the mean-field features generated by turbulence can be captured by the linear analysis as done in neutral fluid physics [13, 14]. However, more effort is required along this line to step towards a conclusion.

Allowing the zonal flow structure to develop by reducing the restoring force acting on the electric potential leads to corrugated profiles with improved confinement, therefore reduced SOL width. Such regimes are characterised by long lived zonal flow patterns [22]. It is to be underlined that the corrugated aspect in terms of the gradients is less pronounced due to the volumetric losses, a feature already reported in Ref.[19]. The analysis of the zonal flow patterns, which is observed to be quite robust, is however modified according to two different time scales. The fast time scale, typical of avalanche transport across the layer, governs a form of modulation in magnitude and position of the zonal flow structure, and consequently of the zonal flow shearing rate. Conversely, a meso-scale slow reorganisation of the pattern can also be noticed, especially in the cases with less developed zonal flow structure, i.e. when the amplitude of the zonal flow pattern is levelled-off by the restoring force acting on the potential.

A major difference with the reported kinetic results [16, 17] is the organisation in space. Kinetic simulations appear to be characterised by a structure with regions that exhibit reduced shear and "free" avalanching transport while the present results exhibit a wave like structure of the zonal flows. The wave length of the pattern seems to be governed by a combination of the damping properties of the zonal flows and inverse cascade of the turbulence that shifts the largest amplitude mode from the injection scale, assuming that is corresponds to the most unstable linear mode, towards larger modes and smaller wave vector. The importance of the damping features in the pattern formation could also explain the specific dynamics of the SOL and its large fluctuation levels. Indeed the properties of the damping terms, enhanced by the parallel losses onto the limiter, determines a narrow window of mode numbers with minimum damping. The reduced number of effective degrees of freedom in this turbulent transport regime would, in a self-consistent way, narrow the range of self-organised patterns and govern larger fluctuation levels. These are particular signatures of SOL turbulent transport, that would then be governed by the specific SOL damping process, namely the volumetric loss terms, in the parallel direction, onto the wall components.

Acknowledgements
This publication has been achieved with the support of the TOP project, which has received funding from Excellence Initiative of Aix-Marseille University- A*MIDEX, a French "Investissements d'Avenir" programme. This work has also been carried out within the framework of the EUROfusion Consortium and has received funding from the Euratom research and training programme 2014-2018 under grant agreement No 633053 for the project ESKAPE, WP17-ENR-CEA-01 as well as WP17-ENR-CEA-021 and WP17-ENR-CEA-03. The views and opinions expressed herein do not necessarily reflect those of the European Commission

References

[1] Rosenbluth M N and Hinton F L 1998 *Phys. Rev. Lett.* **80**(4) 724–727 URL https://link.aps.org/doi/10.1103/PhysRevLett.80.724
[2] Dimits A M, Bateman G, Beer M A, Cohen B I, Dorland W, Hammett G W, Kim C, Kinsey J E, Kotschenreuther M, Kritz A H, Lao L L, Mandrekas J, Nevins W M, Parker S E, Redd A J, Shumaker D E, Sydora R and Weiland J 2000 *Physics of Plasmas (1994-present)* **7** 969–983 URL http://scitation.aip.org/content/aip/journal/pop/7/3/10.1063/1.873896
[3] Physics) E D C T, Database W H C C, Modelling), Pedestal Y K C, Edge), (co Chair Transport Physics) V M, (co Chair Pedestal T O, Edge), (co Chair Confinement Database A P, Modelling), Bateman G, Connor J, (retired) J C, Fujita T, Garbet X, Hahm T, Horton L, Hubbard A, Imbeaux F, Jenko F, Kinsey J, Kishimoto Y, Li J, Luce T, Martin Y, Ossipenko M, Parail V, Peeters A, Rhodes T, Rice J, Roach C, Rozhansky V, Ryter F, Saibene G, Sartori R, Sips A, Snipes J, Sugihara M, Synakowski E, Takenaga H, Takizuka T, Thomsen K, Wade M, Wilson H, Group I T P T, Database I C, Group M T, Pedestal I and Group E T 2007 *Nuclear Fusion* **47** S18 URL http://stacks.iop.org/0029-5515/47/i=6/a=S02
[4] Dif-Pradalier G, Diamond P H, Grandgirard V, Sarazin Y, Abiteboul J, Garbet X, Ghendrih P, Strugarek A, Ku S and Chang C S 2010 *Phys. Rev. E* **82**(2) 025401 URL http://link.aps.org/doi/10.1103/PhysRevE.82.025401
[5] Ghendrih P, Norscini C, Cartier-Michaud T, Dif-Pradalier G, Abiteboul J, Dong Y, Garbet X, Grcan O, Hennequin P, Grandgirard V, Latu G, Morel P, Sarazin Y, Storelli A and Vermare L 2014 *The European Physical Journal D* **68** 303 ISSN 1434-6060 URL http://dx.doi.org/10.1140/epjd/e2014-50210-8
[6] Sarazin Y and Ghendrih P 1998 *Physics of Plasmas* **5** 4214–4228 (*Preprint* https://doi.org/10.1063/1.873157) URL https://doi.org/10.1063/1.873157
[7] Garbet X, Laurent L, Roubin J P and Samain A 1991 *Nuclear Fusion* **31** 967 URL http://stacks.iop.org/0029-5515/31/i=5/a=015
[8] Nedospasov A V 1993 *Physics of Fluids B: Plasma Physics* **5** 3191–3194 (*Preprint* https://doi.org/10.1063/1.860655) URL https://doi.org/10.1063/1.860655
[9] Darmet G, Ghendrih P, Sarazin Y, Garbet X and Grandgirard V 2008 *Communications in Nonlinear Science and Numerical Simulation* **13** 53 – 58 ISSN 1007-5704 vlasovia 2006: The

Second International Workshop on the Theory and Applications of the Vlasov Equation URL http://www.sciencedirect.com/science/article/pii/S1007570407001104

[10] Cartier-Michaud T, Ghendrih P, Sarazin Y, Dif-Pradalier G, Drouot T, Estve D, Garbet X, Grandgirard V, Latu G, Norscini C and Passeron C 2014 *Journal of Physics: Conference Series* **561** 012003 URL http://stacks.iop.org/1742-6596/561/i=1/a=012003

[11] Cartier-Michaud T, Ghendrih P, Sarazin Y, Abiteboul J, Bufferand H, Dif-Pradalier G, Garbet X, Grandgirard V, Latu G, Norscini C, Passeron C and Tamain P 2016 *Physics of Plasmas* **23** 020702 URL http://scitation.aip.org/content/aip/journal/pop/23/2/10.1063/1.4941974

[12] Ghendrih P, Norscini C, Cartier-Michaud T, Dif-Pradalier G, Abiteboul J, Dong Y, Garbet X, Gürcan O, Hennequin P, Grandgirard V, Latu G, Morel P, Sarazin Y, Storelli A and Vermare L 2014 *The European Physical Journal D* **68** 303 ISSN 1434-6079 URL https://doi.org/10.1140/epjd/e2014-50210-8

[13] Malkus W V R 1956 *Journal of Fluid Mechanics* **1** 521–539

[14] Barkley D 2006 *EPL (Europhysics Letters)* **75** 750 URL http://stacks.iop.org/0295-5075/75/i=5/a=750

[15] Norscini C 2015 *Self-organized turbulent transport in fusion plasmas* Theses Université d'Aix Marseille URL https://tel.archives-ouvertes.fr/tel-01296283

[16] Dif-Pradalier G, Hornung G, Ghendrih P, Sarazin Y, Clairet F, Vermare L, Diamond P H, Abiteboul J, Cartier-Michaud T, Ehrlacher C, Estève D, Garbet X, Grandgirard V, Gürcan O D, Hennequin P, Kosuga Y, Latu G, Maget P, Morel P, Norscini C, Sabot R and Storelli A 2015 *Phys. Rev. Lett.* **114**(8) 085004 URL https://link.aps.org/doi/10.1103/PhysRevLett.114.085004

[17] Dif-Pradalier G, Hornung G, Garbet X, Ghendrih P, Grandgirard V, Latu G and Sarazin Y 2017 *Nuclear Fusion* **57** 066026 URL http://stacks.iop.org/0029-5515/57/i=6/a=066026

[18] Ghendrih P, Sarazin Y, Attuel G, Benkadda S, Beyer P, Falchetto G, Figarella C, Garbet X, Grandgirard V and Ottaviani M 2003 *Nuclear Fusion* **43** 1013 URL http://stacks.iop.org/0029-5515/43/i=10/a=001

[19] Floriani E, Ciraolo G, Ghendrih P, Lima R and Sarazin Y 2013 *Plasma Physics and Controlled Fusion* **55** 095012 URL http://stacks.iop.org/0741-3335/55/i=9/a=095012

[20] Ashourvan A and Diamond P H 2016 *Phys. Rev. E* **94**(5) 051202 URL https://link.aps.org/doi/10.1103/PhysRevE.94.051202

[21] Rath F, Peeters A G, Buchholz R, Grosshauser S R, Migliano P, Weikl A and Strintzi D 2016 *Physics of Plasmas* **23** 052309 (*Preprint* https://doi.org/10.1063/1.4952621) URL https://doi.org/10.1063/1.4952621

[22] Gallaire F and Brun P T 2017 *Philosophical Transactions Of The Royal Society A-Mathematical Physical And Engineering Sciences* **375** 44. 20160155